International Journal of Refractory Metals and Hard Materials 143 (2027) 108176

Contents lists available at ScienceDirect

International Journal of Refractory Metals and Hard Materials

journal homepage: www.elsevier.com/locate/IJRMHM

Phase evolution, high-temperature strength and oxidation response of Mo–Si–Ti alloys produced by powder metallurgy route

Ievgen Solodkyi [a,*], Kateryna Khanchych [b], Mihai Alexandru Grigoroscuta [c], Georg Hasemann [a], Ulf Betke [a], Petre Badica [c], Manja Krüger [a]

[a] Otto von Guericke University Magdeburg, Universitätsplatz 2, Magdeburg, 39106, Germany
[b] Karlsruhe Institute of Technology, Institute for Applied Materials – Applied Materials Physics (IAM-AWP), Kaiserstraße 12, Karlsruhe, 76131, Germany
[c] National Institute of Materials Physics, Atomistilor 405 A, Magurele, 077125, Romania

ARTICLE INFO

Keywords:
Mo–Si–Ti alloy
Alloy design
Spark plasma sintering
High temperature compression strength
Oxidation
Phase diagram

ABSTRACT

Molybdenum-based Mo–Si–Ti alloys with a multiphase microstructure were produced via a powder metallurgy route. The effects of the varied silicide fraction Mo-(20–50 vol%Ti_5Si_3) and SPS temperature 1500–1700 °C on the phase evolution of the Mo–Si–Ti alloys were established. The microstructure and chemical composition of individual phases were analyzed. Thermodynamic calculations were performed at the sintering temperatures, and the predicted phase compositions were compared with the experimental results. The oxidation behaviour of the obtained alloys was evaluated at 800 °C and 1100 °C. It was shown that a Ti_5Si_3 fraction of more than 50 vol % is required to ensure oxidation resistance at pesting temperature of 800 °C. Hardness as well as compressive strength in the temperature range of 800–1400 °C were also studied. Owing to the $(Mo,Si,Ti)_{ss}$ matrix, the alloy starts to plastically deform at 800 °C, with a yield strength of about 1200 MPa.

1. Introduction

In the past three decades, molybdenum-based alloys have gained considerable interest as candidates for structural applications in aerospace engines and gas turbines. They have high melting points around 2000 °C and thus may show promise for good creep and oxidation resistance at temperatures up to 1200 °C [1–3]. However, for the intensive use of molybdenum-based alloys, such problems as insufficient strength at elevated temperatures, low-temperature brittleness, and poor oxidation resistance at intermediate temperatures need to be addressed, which are the main concerns for their practical use [4].

Among molybdenum alloys, most attention has been paid to such systems as Mo-Si-B [5,6] and Mo-Si-Ti [5,7]. It has been reported that macro-alloying of Ti in Mo_5Si_3 forms $(Mo, Ti)_5Si_3$ phase possessing superior oxidation resistance at 750–1300 °C [8].

However, current Mo-Si-B alloys require a decrease in specific density compared to Ni-base superalloys, as well as an increase in room temperature fracture toughness [9]. The issue of excessive brittleness at room temperature can be addressed by increasing the fraction of the molybdenum-based solid solution (Mo_{ss}) [10], while enhanced oxidation resistance can be achieved by increasing the fraction of intermetallic phases [11]. The issue of specific density can be solved by adding light elements such as Ti. In addition to solving the above problems, the addition of Ti can improve the high-temperature oxidation behaviour of alloys [12,13]. Subsequently, boron-free Mo-Si-Ti alloys were proposed to improve the resistance to high-temperature oxidation due to the formation of a mixed oxide layer of SiO_2 and TiO_2 [14,15].

Another important aspect and drawback of the widespread use of molybdenum-based alloys is the availability of various technologies for producing products of such alloys. In addition to conventional melting-based processing, powder metallurgy (PM) provides an alternative route for producing Mo-based alloys and may expand the range of attainable compositions and component geometries, potentially reducing material losses and manufacturing costs [16]. Moreover, PM technology may provide a means of influencing the microstructure and phase composition, provided that the initial powder characteristics, particularly the chemical composition, are carefully controlled [17]. This may, in turn, facilitate tailoring of the microstructure after consolidation. Additionally, during the sintering of powder materials, alloying can in-situ occur in the solid phase without melting at high temperatures, i.e. over 2000 °C for Mo-Si-Ti alloys [18,19].

* Corresponding author.
E-mail address: ievgen.solodkyi@ovgu.de (I. Solodkyi).

https://doi.org/10.1016/j.ijrmhm.2026.108176
Received 9 July 2026; Received in revised form 13 October 2026; Accepted 16 October 2026
Available online 20 October 2026
0263-4368/© 2026 The Authors. Published by Elsevier Ltd. This is an open access article under the CC BY license (http://creativecommons.org/licenses/by/4.0/).
Open access funding enabled and organized by Projekt DEAL.

Mechanical alloying (MA) has been effectively used to produce molybdenum-based alloy powders with a dispersed and homogeneous microstructure [14,15,20],[21,22]. After sintering, these powders showed high mechanical strength and good high-temperature oxidation behaviour [17]. However, the long alloying time during the MA process (usually more than 20 h) and the small volume of the resulting powder alloy significantly reduce the effectiveness of this approach. One possible approach to utilizing powder-based starting materials is to employ PM techniques to produce high-density products while simultaneously forming the desired chemical and phase composition of the alloy, as well as its target microstructure, in-situ [17].

Therefore, the aim of this work is to study the influence of the chemical composition of the initial powder mixtures and the parameters of the spark plasma sintering (SPS) process of phase composition, and microstructure formation in the Mo-Si-Ti system. For this purpose, it is proposed to use Mo-Ti_5Si_3 powder mixtures with different fraction of titanium silicide.

2. Material and methods

The starting powders were Mo (2–5 μm, >99.95% purity, ChemPur), Ni (<10 μm, >99.9% purity), and Ti_5Si_3 (99.5% Xi'an function material group Co.,Ltd., China) with a size of <63 μm. To improve the sinterability of the molybdenum matrix of the composite, 1 wt% of Ni powder was added. Small additions of Ni can significantly enhance the densification of Mo by providing a fast diffusion pathway along the Mo particle surfaces and grain boundaries, thereby reducing the effective activation energy for sintering. For example, the addition of Ni was reported to reduce the activation energy for densification of Mo to approximately 143 kJ mol^{-1}, substantially below that associated with bulk Mo diffusion [23]. Ni promotes the formation of a thin Ni-rich/NiMo layer at Mo grain boundaries, which acts as a short-circuit diffusion path and facilitates Mo transport during sintering [24]. A similar beneficial effect of 1 wt% Ni was observed during the sintering of Mo-based composites containing Mo–Si–B intermetallic inclusions, where Ni increased the diffusion rate of Mo and enhanced densification while reducing the Kirkendall porosity [25]. The powder mixtures of Mo + 1 wt% Ni + x Ti_5Si_3 (x = 20; 30; 40; 50 vol%) were prepared by mixing in a planetary ball (Retsch PM100, Germany) mill for 30 min. Mixing was carried out in steel jar with steel balls in an argon environment. The ratio of grinding media to material was 4:1, the rotation speed was 200 rpm. Such mild mixing conditions were used to obtain a homogeneous mixture rather than grinding Ti_5Si_3 particles. The microstructure of the initial mixture, as well as the distribution of the phase components of the composite, is shown in Fig. 1. The samples were labelled taking into account the fraction of Ti_5Si_3 ceramic filler in the initial mixture of powders and the sintering temperature (Table 1).

Spark plasma sintering of powder mixtures was performed using FCT Systeme GmbH–HP D 5 (Effelder-Rauenstein, Germany) equipment. The powder mixture was wrapped in a graphite foil (0.1 mm thick) and loaded into a 20 mm diameter graphite die. The initial pressure of 5 MPa was used. The heating rate was 100 °C/min. Pressure of 63 MPa was applied while the sample was heated and kept constant during the sintering process. The holding time at sintering temperature of 1500–1700 °C was 10 min. During cooling from the holding temperature to 500 °C, the applied pressure was maintained constant. The pressure was reduced only when the temperature reached 500 °C. The sintering process was performed in an argon atmosphere with a flow rate of 2 $L{\cdot}min^{-1}$. In order to maximize the removal of oxygen from the chamber, it was evacuated three times with the chamber filled with argon after each operation.

The microstructure and chemical composition of the polished composites were analyzed using a Zeiss EVO 15 scanning electron microscope equipped with EDS. The EDS measurements were performed using an accelerating voltage of 20 kV. The phase composition of sintered samples was analyzed by X-ray diffraction method using Bruker D8 Discover with CuKα radiation. The phase composition of the sintered samples was analyzed by X-ray diffraction (XRD) using a Bruker D8 Discover diffractometer with Cu Kα radiation. Rietveld refinements were performed using TOPAS V6 (Bruker AXS, Karlsruhe, Germany / Coelho Software, Brisbane, Australia). Rietveld refinements were performed for all six samples using the same refinement strategy. The obtained refinement residuals were R_{wp} = 1.19–1.62%, R_p = 0.92–1.10%, and R_{exp} = 0.91–0.94%, with goodness-of-fit (GOF) values ranging from 1.28 to 1.73. The corresponding χ^2 values were in the range of 1.64–2.99. These values indicate a satisfactory agreement between the experimental and calculated diffraction profiles. The refinement procedure included a 15-parameter polynomial background, specimen-height displacement correction, and independent refinement of the lattice parameters for all identified phases. Crystallite size and microstrain were also refined for all phases. Additionally, the overall phase composition of the sintered alloys was determined by quantitative analysis of digital SEM images using ImageJ software (version 1.54 g; National Institutes of Health, Bethesda, MD, USA). The theoretical density of the composites was first estimated from their quantitative phase composition and the lattice volumes of the constituent phases. However, for most samples, the calculated values resulted in relative densities exceeding 100%. This discrepancy may be attributed to measurement uncertainties and the limited sensitivity of XRD to minor phases. Consequently, it was decided to use only the measured densities of the sintered alloys for further analysis.

Hardness was tested with the Vickers method. The Vickers hardness was measured with an indentation load of 10 kg and a dwell time of 10 s using the Buehler UH250 Vickers Hardness Tester (Leinfelden-Echterdingen, Germany). For accuracy, the samples were polished to a near-mirror finish and checked for face parallelism before testing. At least 10 measurements were performed on each sample.

Samples for oxidation testing were cut from the bulk material into specimens measuring 2 × 2 × 3 mm^3. The oxidation experiments were conducted **in air** at 800 °C and 1100 °C using a laboratory muffle furnace (Labotherm, type L9/S17, Nabertherm, Bremen, Germany). During the first hour, the samples were weighed at 10-min intervals;

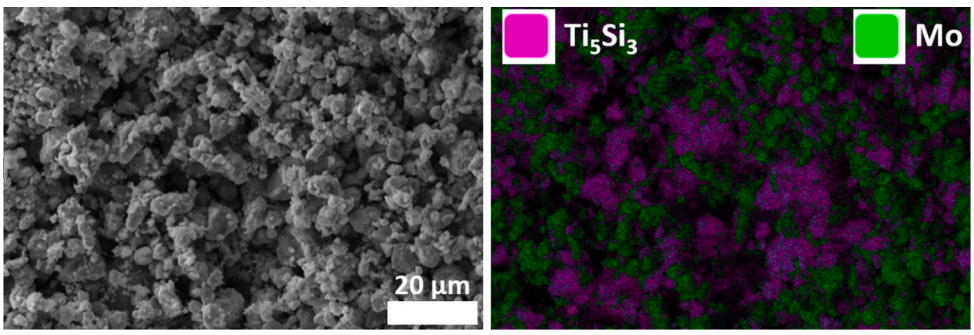


Fig. 1. Morphology of powder particles and distribution of the components in initial mixture of M50TS powders.

Table 1
Results of XRD analysis and properties of sintered samples.

Sample ID	Ti_5Si_3 fraction in powder mixture, vol%	T of SPS, °C	Phase composition after SPS, vol%, (lattice parameter)			Density, g/cm^3	HV10, GPa
			Ti_5Si_3	$(Mo,Ti)_3Si$	$(Mo,Si,Ti)_{ss}$		
M20TS-1500	20	1500	5.0	25.7 (a = 4.9014 Å)	71.3 (a = 3.1492 Å)	9.0 ± 0.1	5.1 ± 0.2
M30TS-1500	30	1500	18.1	25.5 (a = 4.9137 Å)	55.4 (a = 3.1501 Å)	8.6 ± 0.15	5.9 ± 0.25
M40TS-1500	40	1500	24.3	22.2 (a = 4.9234 Å)	55.5 (a = 3.1509 Å)	8.0 ± 0.1	6.9 ± 0.3
M50TS-1500	50	1500	35.2	15.5 (a = 4.9312 Å)	49.3 (a = 3.1518 Å)	7.1 ± 0.1	7.9 ± 0.3
M50TS-1600	50	1600	19.0	38.5 (a = 4.9218 Å)	42.5 (a = 3.1525 Å)	7.5 ± 0.1	9.2 ± 0.5
M50TS-1700	50	1700	10.0	71.3 (a = 4.9263 Å)	18.7 (a = 3.1526 Å)	7.6 ± 0.1	10.8 ± 0.4

subsequently, measurements were performed every 60 min up to 8 h and then every 24 h until the total exposure time reached 100 h. Prior to placing the samples, three for each temperature, in the preheated furnace, their initial mass and dimensions were recorded. The mass was measured using an analytical balance (Sartorius Cubis®, Sartorius AG, Germany) with an accuracy of 0.0001 g. At the end of each cycle, the specimens were removed from the furnace, cooled to room temperature under atmospheric conditions, and carefully weighed to determine the mass change after the corresponding exposure time.

Compression samples with a cross-section of 2 × 2 mm^2 and a height of 3 mm were prepared from the SPS compacts by electro-discharge machining (EDM). Compression tests were carried out in the temperature range of 800–1400 °C under a vacuum of 10^{-5} mbar using a ZwickRoell Kappa 100 SS-CF electromechanical universal testing machine. The tests were performed at a constant crosshead speed corresponding to an initial (engineering) strain rate of $\varepsilon = 10^{-3}$ s^{-1}. At least three samples from each series were tested at each temperature. The compressive plastic strain was determined by subtracting the combined compliance of the testing machine and the specimen from the individually measured load–displacement curves.

Thermodynamic calculations for the Mo-Si-Ti system are performed via FactSage 8.4 software within the CALPHAD framework [26], employing an in-house database together with the pre-installed standard SGTE database for pure elements. The thermodynamic database for Mo-Si-Ti system is based on the phase descriptions reported in [18], which were experimentally validated on two isothermal sections – 1600 °C and 1425 °C. The calculated solid-state phase equilibria are also consistent with the most recent critical evaluation of the Mo-Si-Ti system reported in [27].

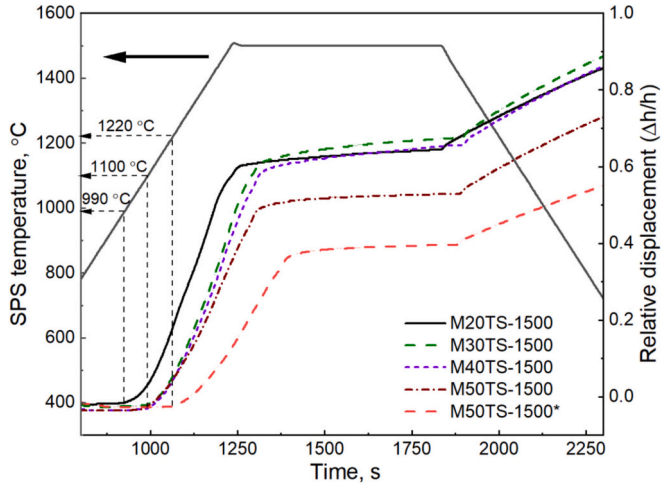


Fig. 2. Punch displacement during SPS at 1500 °C for Mo with varying Ti_5Si_3 powder fraction. M50TS-1500* - densification diagram for the samples without the addition of 1 wt% Ni.

3. Results and discussion

Fig. 2 shows the shrinkage of a powder's mixture with different fraction of Ti_5Si_3. It is quite obvious that with an increased in the fraction of Ti_5Si_3 particles, the material shrinkage begins at higher temperatures. Moreover, one can see a change in the slope of the curve with an increase in the fraction of the ceramic filler, which indicates a decrease in the compaction rate. It should be noted that the shrinkage value for composite mixtures with a Ti_5Si_3 fraction of 20–40 vol% is almost the same magnitude of about 0.65. While for the sample M50TS-1500, the maximum shrinkage is about 0.52. The explanation for this effect will be given below in the discussion of the phase composition of the alloy after sintering. It is worth noting that in order to improve the sinterability of molybdenum-based alloy, 1 wt% Ni was added [24]. To evaluate the effect of 1 wt% Ni on the densification behaviour of the MxTS powder mixture, an additional sintering experiment was conducted without nickel addition for Mo-50vol.%Ti_5Si_3 composition (sample ID M40TS-1500*, Fig. 2). Comparison of the densification diagrams for the powder mixture with and without the addition of 1 wt% clearly indicates a pronounced activation of the compaction process in the presence of Ni. Without Ni addition, shrinkage begins at about 1220 °C, whereas with Ni it starts at approximately 1100 °C. In addition, the total shrinkage with Ni is nearly twice as high. Table 1 presents the density values of the obtained alloys. As the Ti_5Si_3 fraction increases up to 50 vol%, the density of the sintered material decreases from 9.0 to 7.1 g/cm^3. To determine the relative density of the sintered alloys, the theoretical density of the composites was first estimated from their quantitative phase composition and the lattice volumes of the constituent phases. However, for most samples, the calculated values resulted in relative densities exceeding 100%. This discrepancy may be attributed to measurement uncertainties and the limited sensitivity of XRD to minor phases. Consequently, it was decided to use only the measured densities of the sintered alloys for further analysis.

The XRD results for the sintered alloys are presented in Fig. 3. The formation of $(Mo,Ti)_3Si$ phase and the shift of the molybdenum diffraction peaks toward lower angles indicate a reaction between the constituent phases during sintering at 1500–1700 °C. Thus, after sintering, three phases $(Mo,Si,Ti)_{ss}$, $(Mo,Ti)_3Si$, and Ti_5Si_3 were recorded. The formation of the $(Mo,Ti)_3Si$ phase within the the $(Mo,Si,Ti)_{ss}$ matrix of the alloy is likely associated with the intense interaction between fine Ti_5Si_3 particles and Mo during SPS.

Table 1 presents the lattice parameters of the newly formed $(Mo,Ti)_3Si$ and $(Mo,Si,Ti)_{ss}$ phases. With increasing Ti_5Si_3 fraction in the initial mixture, the lattice parameter a of $(Mo,Ti)_3Si$ phase increases up to 4.9312 Å, which is due to the incorporation of Ti into the Mo_3Si lattice. The lattice parameters of the $(Mo,Si,Ti)_{ss}$ phase (Table 1) correspond to the solid solution of Ti in Mo [28,29] and increase with increasing Ti_5Si_3 fraction. The effect of silicon on the lattice parameter was not taken into account. The lattice parameters of the solid-solution phase determined by XRD are in good agreement with the literature data. In particular, the lattice parameter range of 3.1492–3.1526 Å corresponds to a titanium content of 15–30 at.%, whereas the titanium concentration determined by EDS was 15–25 at.%. These values are also in good agreement with data reported for alloys produced by arc melting

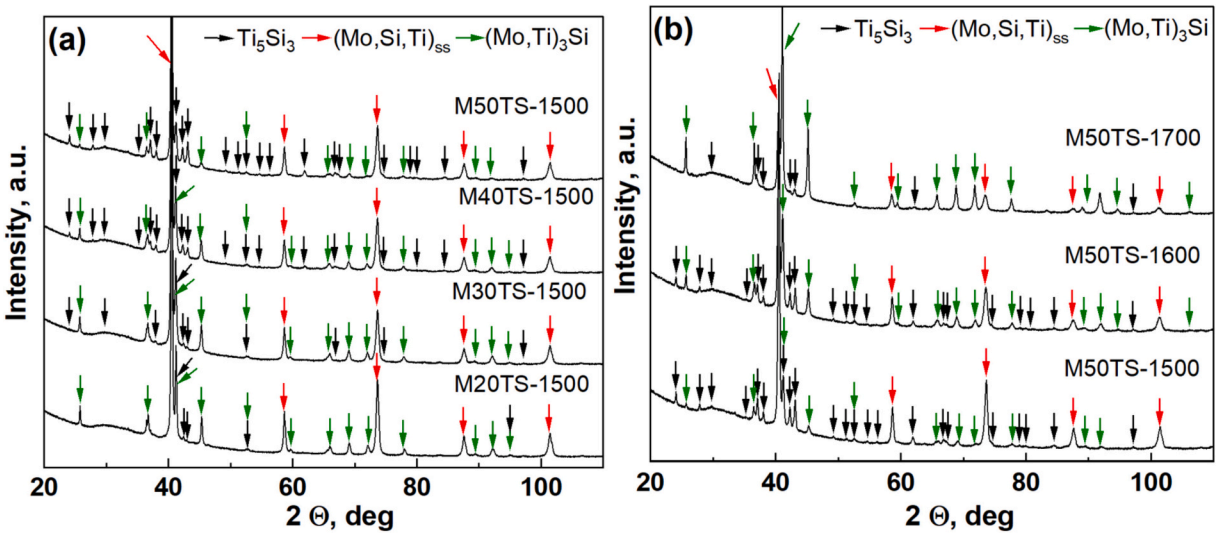


Fig. 3. XRD patterns of subjected to SPS alloys: (a) at 1500 °C with different fraction of Ti_5Si_3 powder in initial mixture and (b) M50TS alloys at different temperatures.

[30].

It should be noted that increasing the SPS temperature at a constant Ti_5Si_3 fraction of 50 vol% also leads to an increase in the lattice parameter of the $(Mo,Ti)_3Si$ phase (Table 1), indicating enhanced Ti solubility at higher sintering temperatures. In addition to changes in phase fractions, both increasing Ti_5Si_3 fraction at 1500 °C and increasing the SPS temperature to 1600 and 1700 °C (at constant 50 vol % Ti_5Si_3) also affect the chemical composition of the phases. This is confirmed by lattice parameter analysis (Table 1), and EDS results for the $(Mo,Si,Ti)_{ss}$ and $(Mo,Ti)_3Si$ phases (Table 2). The relatively large size of these phases (~5–8 μm) enabled reliable compositional analysis. The Si content in the $(Mo,Si,Ti)_{ss}$ phase slightly increases with increasing Ti_5Si_3 fraction and reaches a maximum of about 4 at.% for the Mo-50 vol % Ti_5Si_3 sample sintered at 1500 °C. The obtained values are somewhat higher than those reported for the binary Mo—Si system (i.e. about 0.3–3.3 at.%) [31] However, the presence of Ti should also be taken into account, as it affects the thermodynamic stability of the solid solution and, consequently, shifts the Si solubility limit. An analysis of the isothermal sections of the Mo–Si–Ti phase diagram at 1425 °C and 1600 °C, as well as with our own calculations at 1500 °C–1700 °C, indicates that the solubility of Si in the Mo-rich body centered cubic (BCC) phase increases with increasing Ti content. In addition, the uncertainty associated with SEM–EDS measurements should be considered, particularly due to the overlap of the electron interaction volumes within the analyzed microstructural regions, which may affect the measured elemental concentrations.

The Ti concentration in the $(Mo,Si,Ti)_{ss}$ phase increases monotonically with increasing Ti_5Si_3 fraction and further rises with increasing SPS temperature up to 1700 °C (Table 2). A similar trend is observed for the Mo_3Si phase. Likewise, the Ti content in the $(Mo,Ti)_3Si$ phase increases both with increasing Ti_5Si_3 fraction (at 1500 °C) and with increasing sintering temperature (Table 2). These trends are consistent with the lattice parameter data (Table 1). In contrast, the Si concentration in the $(Mo,Ti)_3Si$ phase varies within approximately 1 at.%, which does not allow for definitive conclusions regarding the influence of composition and temperature. According to the reported data [32], the Si content in the Mo_3Si phase is 24 at.%. In contrast, somewhat higher Si contents were measured in the present study (Table 2). However, as in the case of the (Mo,Si,Ti) phase, the potential influence of Ti on the phase composition should not be disregarded. In addition, the uncertainty associated with the SEM–EDS measurements should be taken into account.

The microstructure of the sintered alloys is shown in Fig. 4. The pores that could be seen in the micrographs were not identified, suggesting a low porosity of the alloys after sintering. Chemical reaction of the phase components of the initial powder mixture is observed for all samples. The analysis of SEM images shows that small particles of Ti_5Si_3 with a size of less than 5 μm are completely transformed into the $(Mo,Ti)_3Si$ phase as a result of interaction with the Mo matrix, while only a rim structure is formed on large particles (Fig. 4 (a)).

Moreover, it should be noted that the alloys sintered at 1500 °C–1600 °C contained particles smaller than 0.5 μm exhibiting pronounced Ti and O signals during SEM-EDS. These particles were therefore considered to be titanium oxide. This phase forms due to the reaction of titanium with oxygen present in the initial powders (450 ppm in Mo and 1910 ppm in Ti_5Si_3). A certain degree of inhomogeneity in titanium oxide particles distribution (marked with light yellow regions) can be observed, which may be attributed to the greater amount of adsorbed oxygen on the surfaces of the finer particles compared with the coarser ones. When the sintering temperature

Table 2
Results of EDS studies of $(Mo,Si,Ti)_{ss}$ and $(Mo,Ti)_3Si$ phases.

Sample ID	EDS results of the phases, at.%					
	$(Mo,Si,Ti)_{ss}$			$(Mo,Ti)_3Si$		
	Mo	Si	Ti	Mo	Si	Ti
M20TS-1500	82.0 ± 1.8	2.7 ± 0.6	15.3 ± 0.8	58.9 ± 1.1	25.5 ± 0.9	15.6 ± 0.9
M30TS-1500	79.2 ± 1.6	3.1 ± 0.5	17.7 ± 0.9	57.2 ± 1.0	25.1 ± 0.9	17.7 ± 0.9
M40TS-1500	77.6 ± 1.6	3.3 ± 0.5	19.1 ± 1.1	53.3 ± 1.3	25.5 ± 1.1	21.2 ± 0.8
M50TS-1500	73.3 ± 1.4	4.0 ± 0.6	22.4 ± 1.4	51.7 ± 1.4	25.7 ± 1.4	22.9 ± 0.6
M50TS-1600	72.7 ± 1.6	3.7 ± 0.6	23.6 ± 1.6	50.1 ± 1.7	26.1 ± 1.5	23.8 ± 0.5
M50TS-1700	72.5 ± 1.5	3.4 ± 0.8	24.1 ± 1.6	48.3 ± 1.8	26.5 ± 1.6	25.2 ± 0.5

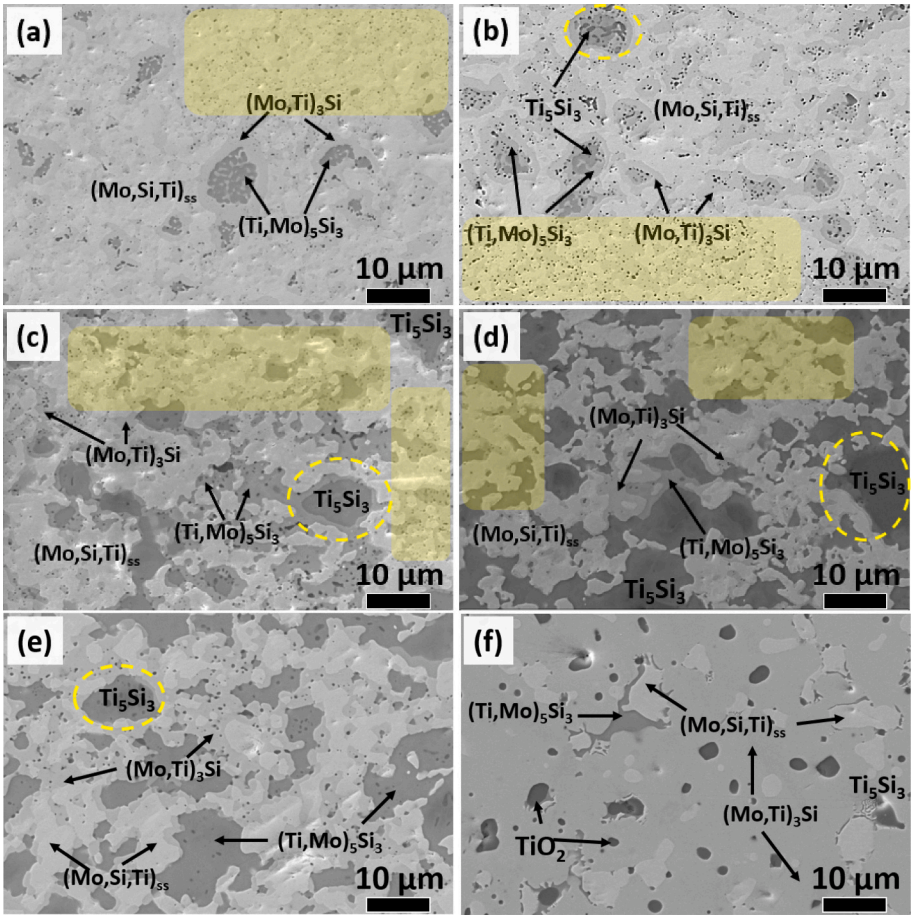


Fig. 4. SEM images of specimens with different fraction of Ti_5Si_3 in the initial powder mixture sintered at 1500 °C: (a) – M20TS; (b) – M30TS; (c) – M40TS; d – M50TS; and of specimens M50TS sintered at (e) – 1600 °C; (f) – 1700 °C.

increases to 1700 °C (Fig. 4(f)), coarsening of the submicron TiO_x particles is observed. At this temperature, overall microstructural coarsening of all phases occurs, associated with the formation of a $(Mo,Ti)_3Si$ matrix containing inclusions of $(Mo,Si,Ti)_{ss}$, $(Ti,Mo)_5Si_3$, Ti_5Si_3, and TiO_x phases. According to thermodynamic calculations (presented below in the text), the temperature at which the liquid phase begins to form is 1936 °C. However, at a sintering temperature of 1700 °C (Fig. 4 (f)), local melting can be observed near unreacted Ti_5Si_3 particles, presumably due to a eutectic reaction.

The predominant distribution of Ti into the Mo-rich phase is primarily governed by the chemical driving force for phase formation and elemental partitioning [33]. Diffusion kinetics control the rate and spatial extent of this redistribution during SPS, facilitating the formation of a Ti-containing Mo-based solid solution and, subsequently, the $(Mo,Ti)_3Si$ phase. In contrast, the formation of the $(Ti,Mo)_5Si_3$ phase is likely associated with Ti-rich local regions, particularly around larger residual Ti_5Si_3 particles, where the local composition and diffusion distances differ from those in finer-particle regions. The microstructure and distribution of chemical elements near the Ti_5Si_3 particles during sintering were additionally investigated (Fig. 5). The redistribution of Ti is primarily driven by the chemical driving force for elemental partitioning, whereas diffusion kinetics determine the rate of this process. Therefore

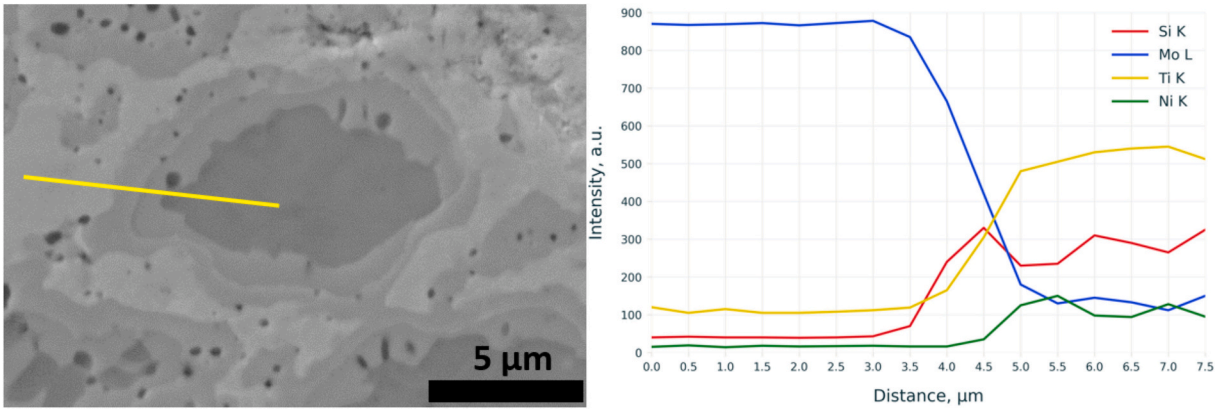


Fig. 5. EDS line-scan analysis across the Mo-Ti5Si3 interface in the M50TS-1500 sintered alloy.

the Ni addition promotes the formation of a thin Ni-rich/Ni–Mo layer at the Mo grain boundaries, which acts as a short-circuit diffusion path and facilitates Mo transport during sintering [24]. The analysis revealed an elevated concentration of nickel in the $(Ti,Mo)_5Si_3$ and Ti_5Si_3 phases (Fig. 5 green line). Furthermore, in our previous work [34], only the formation of a $(Mo,Si,Ti)_{ss}$, and the $(Mo,Ti)_3Si$ phase was observed after nickel-free sintering. Further research is needed to investigate in more detail the effect of nickel on the alloying process in multicomponent Mo-Si-Ti powder systems.

Based on SEM-EDS analysis of sintered samples, the existence of 4 phases $(Mo,Si,Ti)_{ss}$, $(Mo,Ti)_3Si$, $(Ti,Mo)_5Si_3$, and Ti_5Si_3 was recorded. To account for the fraction of all phases and their variation depending on the Ti_5Si_3 fraction and sintering temperature, the quantitative phase composition was determined by analysing microstructural images. Fig. 6 (a) shows the variation in phase composition as a function of the Ti_5Si_3 particles fracture in the initial mixture and the SPS temperature.

The observed phase evolution indicates that the sintered alloys do not represent an equilibrium phase assemblage, but rather a kinetically controlled state resulting from the reaction between the initial Mo and Ti_5Si_3 powders during SPS. Interdiffusion of Mo, Ti, and Si across the initial phase interfaces promotes the formation of the ternary $(Mo,Ti)_3Si$ phase, accompanied by a reduction in the fractions of both Ti_5Si_3 and the $(Mo,Si,Ti)_{ss}$ matrix. Increasing the Ti_5Si_3 fraction in the initial mixture up to 30 vol% results in an increase in the amount of $(Mo,Ti)_3Si$, whereas a further increase to 40–50 vol% leads to a decrease in its fraction. This non-monotonic behaviour reflects the changing relative amounts of the reacting phases and the diffusion-controlled nature of the reaction. The formation of $(Mo,Ti)_3Si$ is also strongly affected by the SPS temperature. Increasing the temperature from 1600 °C to 1700 °C results in a significant increase in the $(Mo,Ti)_3Si$ fraction from 38.5 to 71.3 vol% (Fig. 6 (b)), accompanied by a decrease in the Ti_5Si_3 fraction from 19.0 to 10.0 vol% and in the $(Mo,Si,Ti)_{ss}$ matrix fraction from 42.5 to 18.7 vol%. These changes indicate that increasing the temperature accelerates interdiffusion and promotes the reaction between Mo and Ti_5Si_3, thereby driving the microstructure further away from the initial phase assemblage. Therefore, the formation of the $(Mo,Ti)_3Si$ phase can be regarded as an inherent consequence of using pure Mo and Ti_5Si_3 powders as the starting materials. Modification of the starting powder chemistry, for example by replacing pure Mo with a pre-alloyed (Mo,Ti) solid solution, may provide a means of reducing the formation of this additional phase.

To better understand the effect of the initial chemical composition and sintering temperature on the equilibrium phase constitution of the investigated alloys, thermodynamic calculations were performed using FactSage 8.4 with an in-house database. The results are presented in Figs. 7 and 8 and in Table 3.

Fig. 7 presents the calculated phase constitution of the alloys with nominal concentrations corresponding to MxTS (x = 20,30,40 and 50 vol%) in the temperature range from 1500 °C up to complete melting. According to the equilibrium calculations, in the sintering temperature range 1500–1700 °C (shaded area), the alloys M20TS, M30TS and M40TS consist of two phases – BCC and $(Mo,Ti)_3Si$, whereas alloy M50TS undergoes a phase transition from a two-phase field BCC+$(Ti,Mo)_5Si_3$ into a three-phase field BCC+$(Ti,Mo)_5Si_3$ + $(Mo,Ti)_3Si$ at 1570.8 °C. The calculated mole fractions of the phases are presented in Table 3.

Fig. 8 shows the calculated isothermal sections of the Mo-Si-Ti system at 1500, 1600 and 1700 °C. It can be seen that compositions containing **20–40 vol%** Ti_5Si_3 are located within the two-phase region of the Mo solid solution (BCC) and $(Mo,Ti)_3Si$. The alloy with 50 vol% Ti_5Si_3 at 1500 °C is located within another two-phase region of BCC and $(Ti,Mo)_5Si_3$ and at 1600 and 1700 °C within a three-phase region of BCC, $(Ti,Mo)_5Si_3$ and $(Mo,Ti)_3Si$. It should be noted, however, that the sintering of the powder samples cannot be considered an equilibrium process. A good example is the presence of residual primary Ti_5Si_3 after sintering in all samples, as evidenced by the XRD results (Table 1). Even when the unreacted Ti_5Si_3 is taken into account, the overall composition of the alloys shifts toward the Mo-rich corner. At the same time, after sintering, samples 1–3 contained the $(Ti,Mo)_5Si_3$ phase (Fig. 6), which,

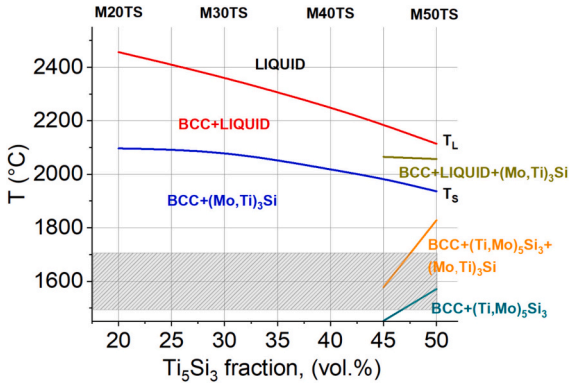


Fig. 7. Calculated phase constitution of the alloys MxTS with x = 20,30,40 and 50 vol%. BCC corresponds to $(Mo,Si,Ti)_{ss}$ phase. Shaded area represents sintering temperatures. T_S - solidus temperature, T_L - liquidus temperature.

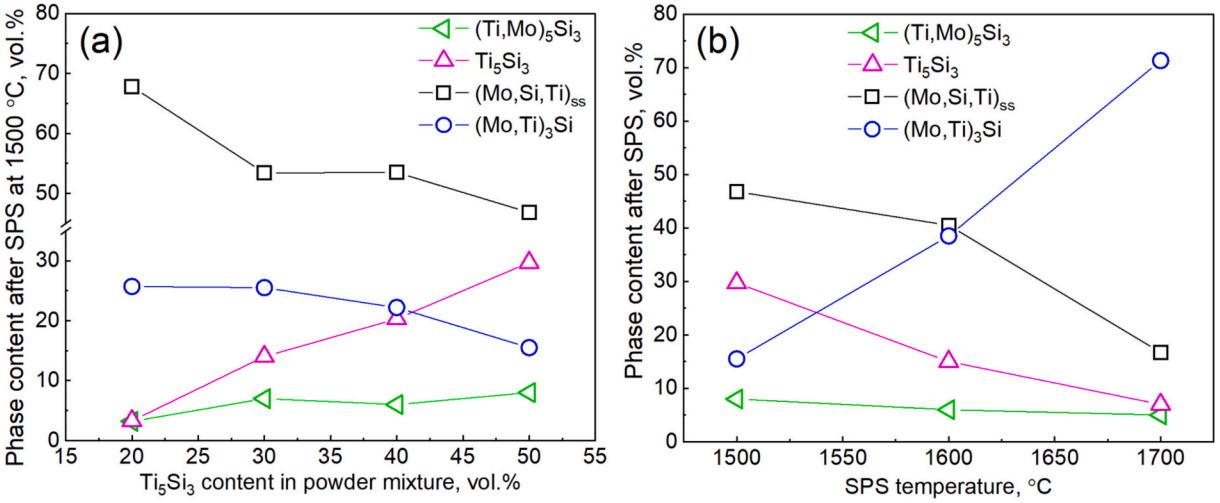


Fig. 6. The variation in phase composition of the alloys: (a) sintered at 1500 °C depending on the fraction of Ti_5Si_3 in the initial mixture and (b) M50TS depending on the SPS temperature.

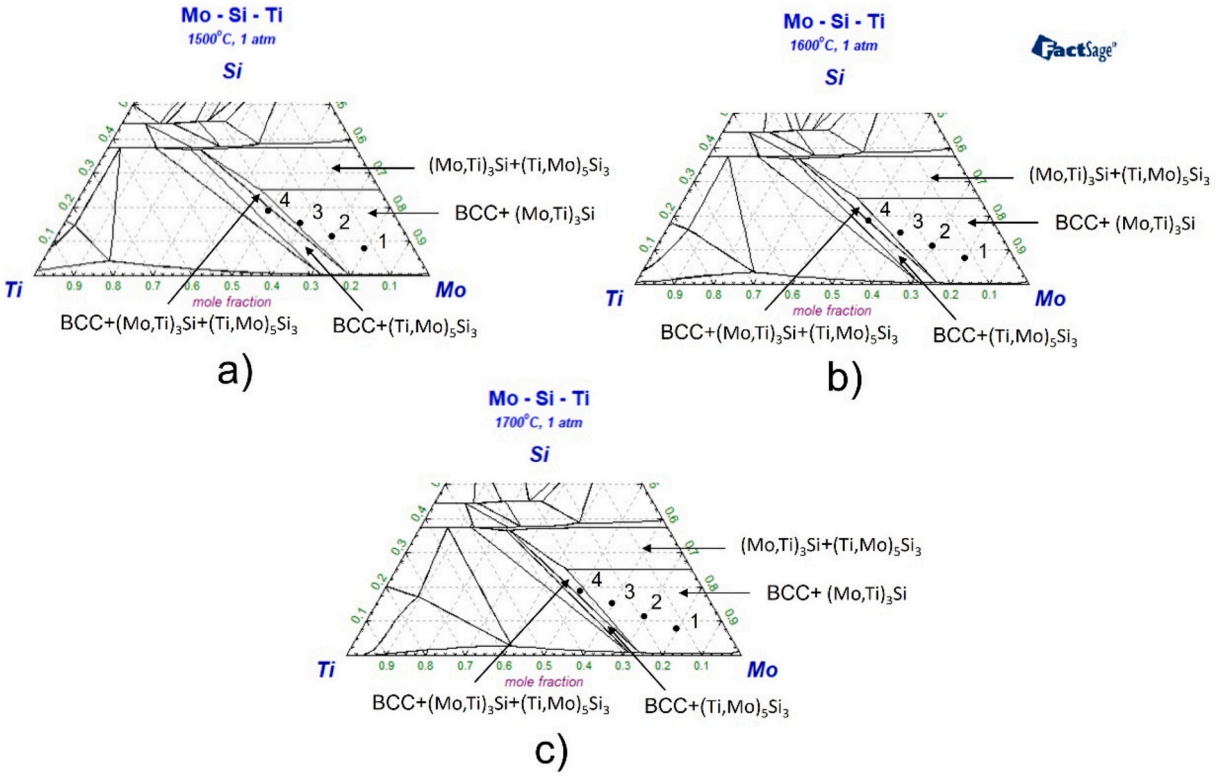


Fig. 8. Calculated isothermal sections of the Mo–Ti–Si system at the SPS temperatures of 1500 (a), 1600 (b), and 1700 °C (c). The numbers 1–4 indicate the alloy compositions corresponding to the initial powder mixtures: 1 – Mo–20 vol%Ti_5Si_3; 2 – Mo–30 vol%Ti_5Si_3; 3 – Mo–40 vol%Ti_5Si_3; and 4 – Mo–50 vol%Ti_5Si_3.

Table 3
Calculated phase constitution of the investigated alloys at various sintering temperatures.

SPS Temperature (°C)	Composition, mole fractions		
	BCC $(Mo,Si,Ti)_{ss}$	$(MoTi)_3Si$	$(Ti,Mo)_5Si_3$
	Mo-12.5Ti-7.5Si (at.%) - M20TS		
1500	0.70	0.30	0
	Mo-18.7Ti-11.3Si (at.%) - M30TS		
1500	0.55	0.45	0
	Mo-25.0Ti-15.0Si (at.%) - M40TS		
1500	0.40	0.60	0
	Mo-31.2Ti-18.7Si (at.%) - M50TS		
1500	0.496	0	0.504
1570.8*	0.4963	0	0.5037
1600	0.46	0.12	0.42
1700	0.35	0.45	0.12

* Temperature at which the $Mo(Ti)_3Si$ phase becomes stable in Mo-31.2Ti-18.7Si (at.%).

according to the calculations, is characteristic only of sample 4 at sintering temperatures above 1570.8 °C (Table 3). This provides further evidence of the non-equilibrium nature of the sintering process, with the local conditions favoring the formation of the $(Ti,Mo)_5Si_3$ phase near the Ti_5Si_3 particles and the $(Mo,Ti)_3Si$ phase near the Mo particles. The calculations also show (Table 3) that increasing the Ti_5Si_3 content in the initial mixture to 40 vol% should result in an increase in the amount of (Mo,Ti)3Si, whereas the experimentally determined phase compositions after sintering show the opposite trend, namely, a decrease in the fraction of $(Mo,Ti)_3Si$ with increasing Ti_5Si_3 content in the initial mixture (Fig. 6). Thus, in contrast to the thermodynamic calculations, which clearly distinguish the two-phase region $(Mo,Si,Ti)_{ss}$ + $(Mo,Ti)_3Si$ from the three-phase region $(Mo,Si,Ti)_{ss}$ + $(Mo,Ti)_3Si$ + $(Ti,Mo)_5Si_3$, the boundary between these regions becomes indistinct during SPS. Nevertheless, the lowest fraction of $(Mo,Ti)_3Si$ after sintering for the sample containing 50 vol% Ti_5Si_3 in the initial mixture is supported by the calculated data, which predict the appearance of this phase only at temperatures above 1570.8 °C. Considering the specific features of SPS [35], it can be assumed that local overheating occurred within the sample during sintering, leading to the formation of the $(Mo,Ti)_3Si$ phase.

It should also be noted that the calculated phase fractions at the higher sintering temperatures of 1600 °C and 1700 °C are in good agreement with the experimental data, which show a sharp increase in the fraction of $(Mo,Ti)_3Si$ phase with increasing sintering temperature. Therefore, in future processing, the use of the lowest possible sintering temperature that still ensures the production of a highly dense material should be considered in order to minimize, or potentially eliminate, the formation of the $(Mo,Ti)_3Si$ phase.

Based on the microstructural investigation (Fig. 4), phase analysis (Figs. 3 and 6), and local chemical analysis (Table 2 and Fig. 5) of the sintered alloys, a schematic illustration of the microstructure and phase composition evolution during sintering was proposed (Fig. 9). It can be observed that an increase in sintering temperature directly affects the amount of the $(Mo,Ti)_3Si$ phase, its increase suppresses the formation of the $(Ti,Mo)_5Si_3$ phase. Moreover, the $(Mo,Ti)_3Si$ phase takes over from the $(Mo,Si,Ti)_{ss}$ phase in forming the structural framework. Owing to their higher reactivity, the finer Ti_5Si_3 particles act as nucleation sites for the formation of the $(Mo,Ti)_3Si$ phase. In contrast, the larger particles remain until the end of sintering and support the formation of the $(Ti,Mo)_5Si_3$ phase.

The Vickers hardness (HV10) of the alloys increases from 5.1 GPa to 7.9 GPa with increasing Ti_5Si_3 fraction (Table 1). A further increase in hardness to 10.8 GPa is observed when the SPS temperature is raised to 1700 °C. This improvement is associated with a significant increase in the volume fraction of the $(Mo,Ti)_3Si$ phase (Fig. 6(b)), which likely contributes to the enhanced hardness.

Fig. 10 presents the results of cyclic oxidation tests at 800 and 1100 °C. During oxidation test at 800 °C, the MT50–1500 sample

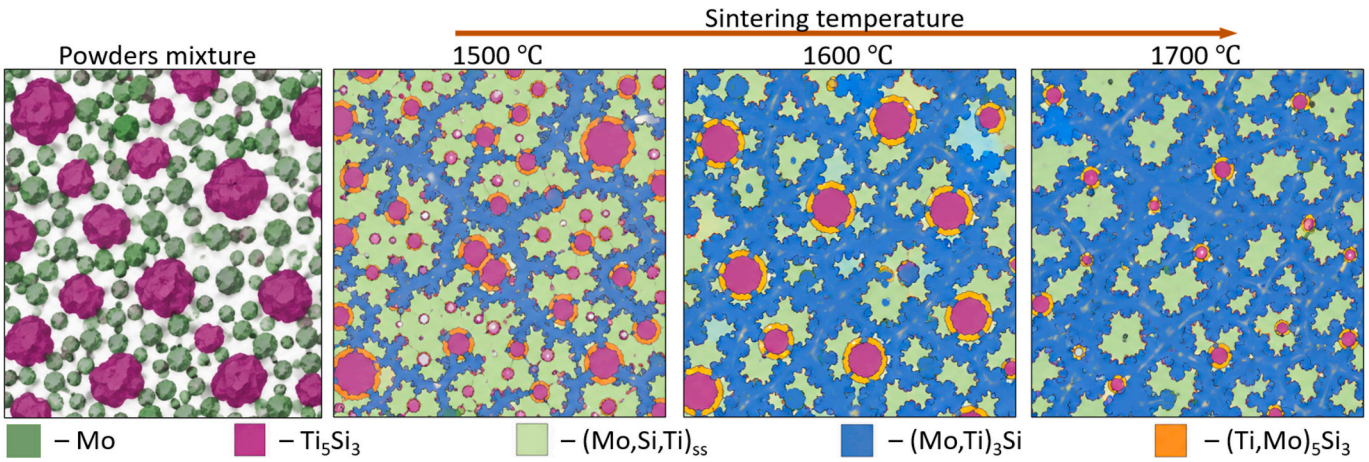


Fig. 9. Schematic illustration of the microstructure and phase evolution during spark plasma sintering of Mo-Ti_5Si_3 powder mixture at temperatures of 1500–1700 °C.

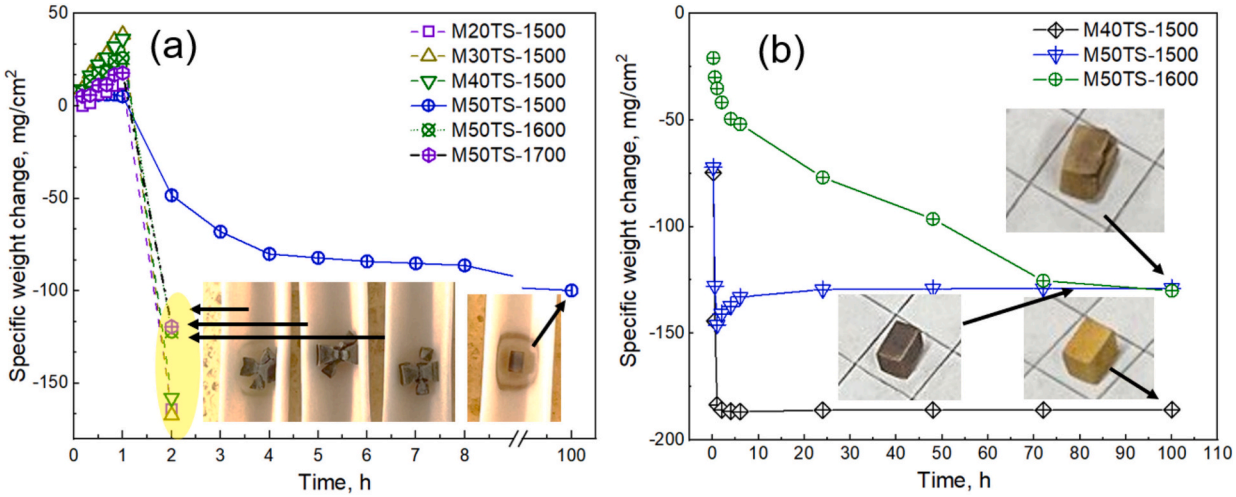


Fig. 10. Cyclic oxidation experiments of the investigated alloys at 800 °C (a) and 1100 °C (b). The insets show macro photographs of the samples after testing, illustrating the character of the fracture.

underwent complete conversion to molybdenum oxide. Although the MT50–1500 specimen did not fracture, the MT20–1500, MT30–1500, and MT40–1500 samples exhibited catastrophic oxidation behaviour (Fig. 10(a), insets), so-called "pesting" as this phenomenon is well-known for Mo-rich alloys [4,11]. Considering the phase composition (Fig. 6), microstructure (Fig. 4), and oxidation behaviour at 800 °C (Fig. 10(a)), it can be concluded that increasing the Ti_5Si_3 phase fraction to 50 vol%, and likely higher, tends to prevent catastrophic alloy failure via the "pesting" mechanism. For oxidation at 1100 °C, samples M40TS-1500 and M50TS-1600 were selected due to their similarity in composition to M50TS-1500 (Table 1), which showed the best performance at 800 °C. As at the oxidation temperature of 800 °C, the sample with the highest fraction of the Ti_5Si_3 ceramic phase M50TS-1500 showed the best stability and remained intact after being exposed at 1100 °C for 100 h (Fig. 10(b)). Analysis of the mass change curve for M50TS-1500 sample (Fig. 6(b)), suggests that intensive MoO_3 evaporation occurs during the first two hours. After 2 h, no continuous protective oxide layer is observed (Fig. 11(a)), which corresponds to a sharp mass loss of nearly −150 mg/cm^2 (Fig. 10(b)). Instead, the oxidized zone consists of a porous composite structure, where a TiO_x/SiO_x matrix contains Ti_5Si_3 inclusions. Subsequently, sufficient amounts of titanium and silicon oxides accumulate on the surface, forming a protective layer, as indicated by the transition to mass gain Fig. 11. After 6 h of oxidation at 1100 °C, the mass change became positive, increasing from approximately +10 mg/cm^2 to +18 mg/cm^2 (Fig. 10(b)). As shown in Fig. 11 (b), a dense TiO_x layer forms on the surface, beneath which a porous structure of TiO_x and SiO_x develops. Notably, the porosity decreases closer to the dense TiO_x layer (see SE image in Fig. 11(b)), suggesting progressive sealing of the initially porous oxide scale. Presumably the relatively coarse initial microstructure and the insufficient Ti content in the $(Mo,Si,Ti)_{ss}$ phase likely delayed the formation of a continuous, more protective scale, resulting in a total oxide-scale thickness of approximately 600 μm after 6 h at 1100 °C.

Thus, to improve the oxidation resistance of the alloys, the Ti content in the $(Mo,Si,Ti)_{ss}$ n phase should be maintained at no less than 40 at.% [19,30]. This may be achieved by increasing the amount of Ti_5Si_3 fraction of and/or reducing its initial particle size to the submicron range. Reducing the particle size would increase its reactivity during sintering, thereby enabling lower sintering temperatures and a finer grain size. In addition, it is expected that decreasing the sintering temperature while keeping other processing parameters constant will result in a reduction in the fraction of the Mo_3Si phase.

Currently, based on the Ti contents in the $(Mo,Si,Ti)_{ss}$ phase after sintering (Table 1), a Ti_5Si_3 fraction of up to 80 vol% in a raw powder mixture would be required. It is therefore considered more appropriate to reduce the initial size of the Ti_5Si_3 particles or/and to use (Mo,Ti)

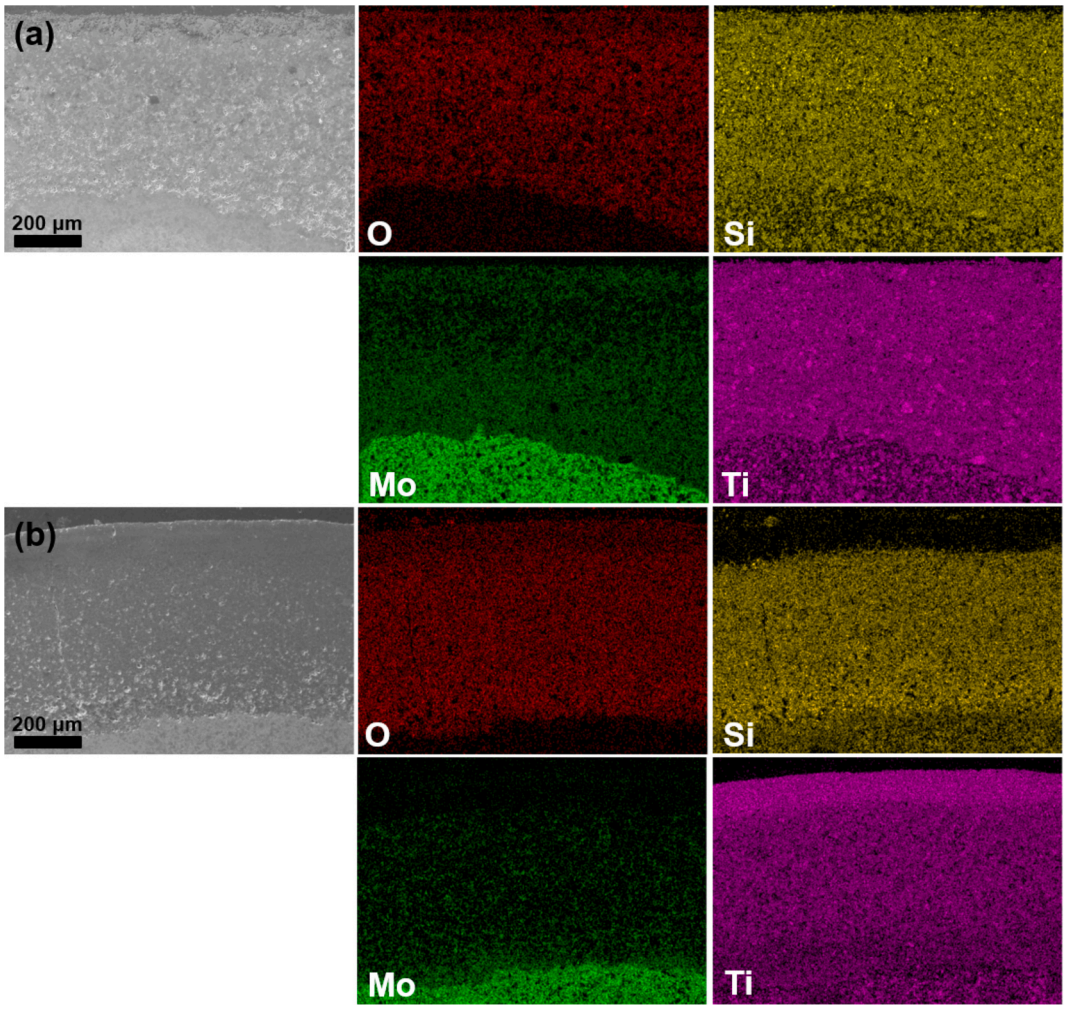


Fig. 11. EDS mapping of chemical elements on the cross-section of the M50TS-1500 sample after oxidation tests at 1100 °C for (a) 2 h and (b) 6 h.

solid solution powder [36].

The M50TS-1500 specimen was selected for the high-temperature strength testing, as it exhibited the best oxidation behaviour. The results are presented in Fig. 12(a). This alloy with approximately 50 vol% of the $(Mo,Si,Ti)_{ss}$ matrix phase provides a certain level of ductility at 800 °C. At 1000 °C and above, the sample undergoes pronounced plastic deformation, reaching a plastic strain exceeding 15%.

It is known that the Ti_5Si_3 phase exhibits strong anisotropy in thermal expansion [37]. In polycrystalline materials, this anisotropy can lead to the development of residual stresses during cooling, potentially

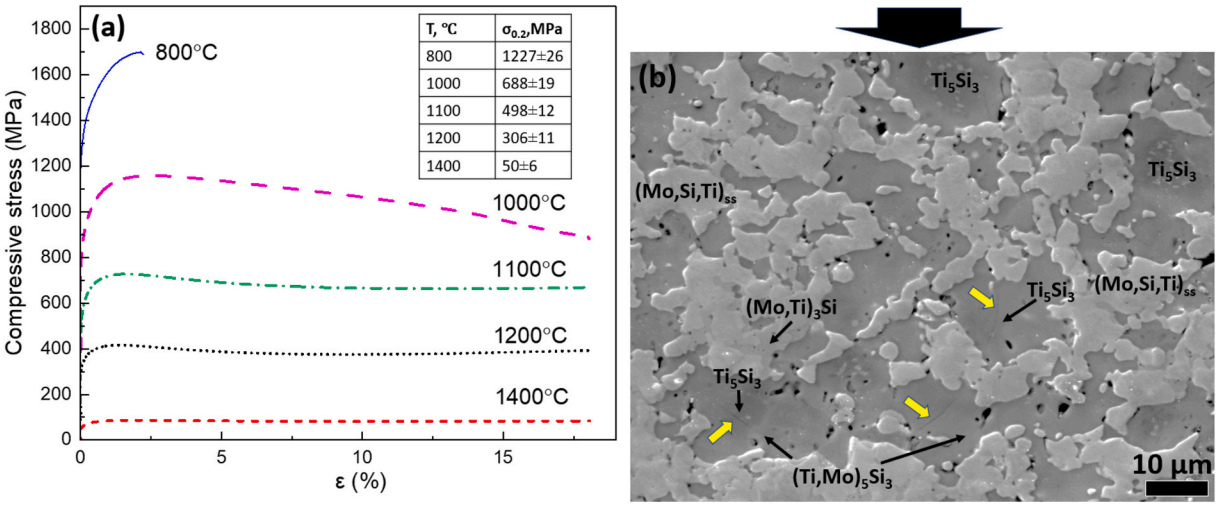


Fig. 12. High temperature compressive stress-strain (a) and microstructure of cross-section after compression test at 1200 °C (b) of the M50TS-1500 sample. The arrow shows the direction of the loading during the compressive strength measurement.

causing microcracking [38]. However, no such microcracks were observed in the dense sintered samples (Fig. 4). Cracks appeared only after compression testing and were predominantly located in Ti_5Si_3 regions (Fig. 12(b)). These cracks tend to close as they approach the (Mo,Si,Ti)$_{ss}$ matrix and/or the (Ti,Mo)$_5Si_3$ phase, which forms a rim around the primary Ti_5Si_3 grains (Fig. 4(c)). Previous studies [37] have shown that alloying Ti_5Si_3 with metallic elements can reduce thermal expansion anisotropy if the alloying atoms differ in size from Ti. Although Mo is not ideal in this respect, the presence of the (Ti,Mo)$_5Si_3$ rim phase may still influence stress distribution around Ti_5Si_3 grains.

The crack propagation is clearly visible in Fig. 13, which was taken after compression tests at 800 °C of the M50TS-1500 sample. In addition to the behaviour of the (Mo,Si,Ti)$_{ss}$ matrix phase (yellow oval) and (Ti,Mo)$_5Si_3$ phase (yellow rectangle) in crack deflection and arrest, plastic behaviour can be observed (red arrows), which is also reflected in the stress-strain curve (Fig. 12(a)).

The yield strength is approximately 1200 MPa at 800 °C and gradually decreases to 680 MPa and 500 MPa at 1000 °C and 1100 °C, respectively (Fig. 14). A further increase in temperature to 1200 °C and 1400 °C reduces the yield strength to approximately 300 MPa and 50 MPa, respectively. The compressive strength values obtained at 1000–1100 °C are in good agreement with those reported for the Mo-20Si-52.8Ti alloy [39], which contains a similar fraction (~50 vol%) of the (Mo,Si,Ti)$_{ss}$ matrix strengthened by the (Ti,Mo)$_5Si_3$ phase. Despite the finer grain size of the Mo-20Si-52.8Ti (DED) alloy [39], the M50TS-1500 alloy exhibits higher strength, most likely due to its more complex hierarchical microstructure and multiphase constitution ((Mo,Ti,Si)$_{ss}$-(Ti,Mo)$_5Si_3$ [39] vs. (Mo,Ti,Si)$_{ss}$-(Ti,Mo)$_5Si_3$-(Mo,Ti)$_3$Si-Ti_5Si_3). The observed difference in strength at elevated temperatures may be associated with the higher Ti content in the (Mo,Si,Ti)$_{ss}$ phase reported in [39]. The increased Ti content lowers the homologous temperature and, consequently, affect the high-temperature strength. Further investigation is therefore required to clarify the effect of Ti content in the (Mo,Si,Ti)$_{ss}$ phase on the high-temperature strength of the alloy. In contrast, the finer microstructure produced by MA followed by sintering provides the Mo-8.9Si-7.7B + La [40], containing approximately 50 vol% Mo$_{ss}$, with a higher yield strength at elevated temperatures. Nevertheless, it is noteworthy that the M50TS-1500 alloy exhibits a compressive ductility of approximately 2.**5% at 800 °C** (Fig. 12(a)), whereas comparable **Mo-Si-B** alloys [40,41] remain brittle under similar conditions.

4. Conclusions

Dense Mo-Si-Ti alloys with a multiphase structure, consisting of a

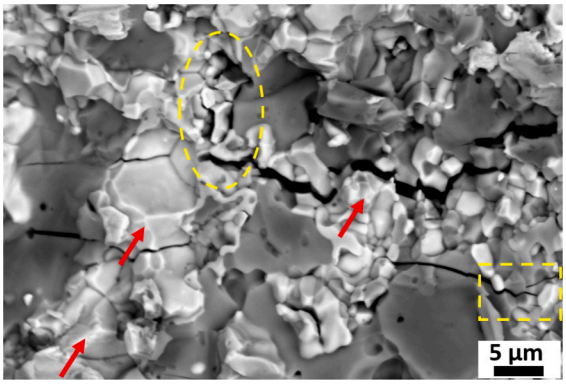


Fig. 13. SEM micrographs of fracture surface after compression test at 800 °C of the M50TS-1500 sample. The yellow oval indicates the deflection and arrest of the crack after contact with the (Mo,Si,Ti)$_{ss}$ matrix phase. The yellow rectangle shows the deflection of the crack and its arrest in the fine-grained (Mo,Si,Ti)$_{ss}$ and (Ti,Mo)$_5Si_3$ phases. The red arrows indicate the plasticity of the matrix material. (For interpretation of the references to colour in this figure legend, the reader is referred to the web version of this article.)

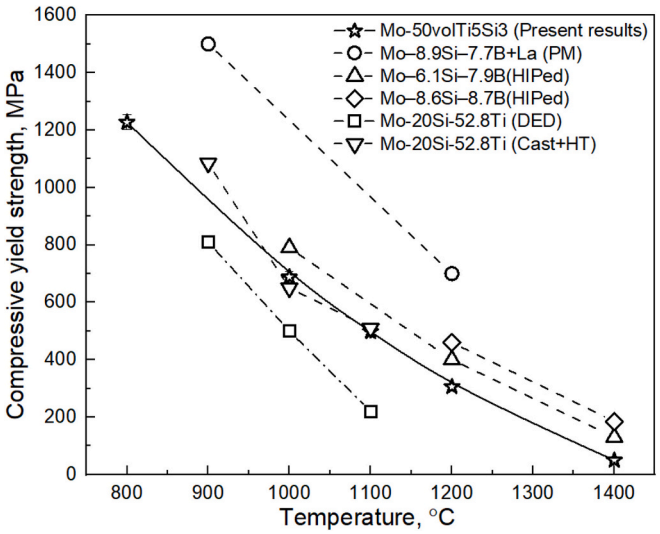


Fig. 14. Temperature-dependent yield strength of the M50TS-1500 alloy in comparison with: Mo–8.9Si–7.7B + La [40], Mo–6.1Si–7.9B(HIPed) and Mo–8.6Si–8.7B(HIPed) [41], Mo-20Si-52.8Ti (DED) [39], Mo-20Si-52.8Ti (Cast+HT) [39].

(Mo,Si,Ti)$_{ss}$ matrix and intermetallic phases (Mo,Ti)$_3$Si, (Ti,Mo)$_5Si_3$, and Ti_5Si_3, were fabricated using spark plasma sintering of Mo-(20–50 vol% Ti_5Si_3) powder mixture at temperatures of 1500–1700 °C. Adding 1 wt% Ni allowed to intensify the densification and obtain almost fully-dense material.

The phase composition and microstructure strongly depend on the Ti_5Si_3 fraction in the initial powder mixture and the SPS temperature. Increasing the Ti_5Si_3 fraction up to 30 vol% promotes the formation of (Mo,Ti)$_3$Si, whereas further increase to 40–50 vol% reduces its fraction. Raising the SPS temperature to 1700 °C results in a higher fraction of (Mo,Ti)$_3$Si and microstructural coarsening. A comparison of the experimentally determined phase composition with the calculated data showed that the sintered alloys do not represent an equilibrium phase assemblage, but rather a kinetically controlled state resulting from the reaction between the initial Mo and Ti_5Si_3 powders during SPS.

A high volume of Ti_5Si_3 particles (above 50 vol%) is essential for oxidation resistance at 800 °C, preventing catastrophic pesting. However, a higher fraction of this Ti_5Si_3 in the starting mixture and/or an increase in its reactivity through grinding is necessary to increase the Ti content in the (Mo,Si,Ti)$_{ss}$ phase after sintering. Meanwhile, to reduce the content of (Mo,Ti)$_3$Si phase, the sintering temperature should be lowered. Furthermore, modifying the chemical composition of the starting powder, for example, by replacing pure Mo with a pre-alloyed solid solution (Mo,Ti) may be a way to reduce the formation of this additional phase.

A composite containing approximately 50 vol% of a (Mo,Si,Ti)$_{ss}$ matrix exhibits plastic deformation at temperatures ≥800 °C. In the 1000–1400 °C temperature range, it exhibits plastic deformation of more than 15%, while maintaining a high yield strength (approximately 700 MPa at 1000 °C). Despite the anisotropy of thermal expansion of Ti_5Si_3, no microcracking was observed in the as-sintered samples. Cracks form only after mechanical loading and are mainly localized within Ti_5Si_3 regions, while the (Mo,Si,Ti)$_{ss}$ matrix and (Ti,Mo)$_5Si_3$ phase contribute to crack arrest. The strengthening mechanism is attributed to the crack-deflection and crack-arrest effects induced by the heterogeneous multiphase microstructure. When a propagating crack encounters the (Mo,Si,Ti)$_{ss}$ matrix phase, its path is deflected and subsequently arrested. In fine-grained regions containing (Mo,Si,Ti)$_{ss}$ and (Ti,Mo)$_5Si_3$ phases, phase and grain boundaries act as effective barriers to crack propagation.

The developed alloys, produced using powder metallurgy,

demonstrate a successful combination of high-temperature strength, ductility, and the potential for improved oxidation resistance, making them promising candidates for use in high-temperature environments.

CRediT authorship contribution statement

Ievgen Solodkyi: Writing – review & editing, Writing – original draft, Visualization, Validation, Supervision, Methodology, Investigation, Formal analysis, Data curation, Conceptualization. **Kateryna Khanchych:** Writing – review & editing, Validation, Methodology, Investigation, Formal analysis, Data curation. **Mihai Alexandru Grigoroscuta:** Methodology, Investigation. **Georg Hasemann:** Writing – review & editing, Writing – original draft, Methodology. **Ulf Betke:** Methodology, Investigation, Data curation. **Petre Badica:** Resources, Methodology, Funding acquisition, Formal analysis. **Manja Krüger:** Writing – review & editing, Writing – original draft, Supervision, Funding acquisition, Conceptualization.

Declaration of competing interest

The authors declare that they have no known competing financial interests or personal relationships that could have appeared to influence the work reported in this paper.

Acknowledgements

This work was partly supported by the German Federal Ministry for Economic Affairs and Climate Action within the framework of the "RACe" project (funding nb. 20E2112A), part of the "Disruptive Technologies and innovative Systems" program.

Support from the DFG, German Research Foundation, as part of the "Major Research Instrumentation Program and the part of Saxony Anhalt is gratefully acknowledged grant 426603139 Bruker D8 Discover XRD. The mechanical testing was conducted using a universal testing machine Zwick/Roel Kappa 100 SS-CF funded by both the DFG, German Research Foundation, as part of the "Major Research Instrumentation Programme" (DFG grant nb. 466497412; INST 272/318-1 FUGG) and the federal state of Saxony-Anhalt.

MAG and PB acknowledge support from UEFISCDI, Romania through project 98PCE/2025 (CCOS).

Data availability

Data will be made available on request.

References

[1] D.L. Anton, E. Hartford, D.M. Shah, P. Whitney, High temperature properties of refractory intermetallics, MRS Online Proc. Libr. 213 (1990) 733, https://doi.org/10.1557/PROC-213-733.
[2] H.-J. Shi, C. Korn, G. Pluvinage, High temperature isothermal and thermomechanical fatigue on a molybdenum-based alloy, Mater. Sci. Eng. A 247 (1998) 180–186, https://doi.org/10.1016/S0921-5093(97)00763-6.
[3] K. Pan, Y. Yang, S. Wei, H. Wu, Z. Dong, Y. Wu, S. Wang, L. Zhang, J. Lin, X. Mao, Oxidation behavior of Mo-Si-B alloys at medium-to-high temperatures, J. Mater. Sci. Technol. 60 (2021) 113–127, https://doi.org/10.1016/j.jmst.2020.06.004.
[4] T. Parthasarathy, M. Mendiratta, D. Dimiduk, Oxidation mechanisms in Mo-reinforced Mo5SiB2(T2)–Mo3Si alloys, Acta Mater. 50 (2002) 1857–1868, https://doi.org/10.1016/S1359-6454(02)00039-3.
[5] M. Zhao, W. Ye, M. Zhu, Y. Gui, W. Guo, S. Wu, Y. Yan, From Mo-Si-B to Mo-Ti-Si-B alloys: a short review, Materials 16 (2022), https://doi.org/10.3390/ma16010003.
[6] K. Yakang, C. Wang, X. Chen, Y. Qu, J. Yu, H. Ju, X. Yilei, Review of research progress on Mo-Si-B alloys, Materials 16 (2023), https://doi.org/10.3390/ma16155495.
[7] D. Schliephake, A. Kauffmann, X. Cong, C. Gombola, M. Azim, B. Gorr, H.-J. Christ, M. Heilmaier, Constitution, oxidation and creep of eutectic and eutectoid Mo-Si-Ti alloys, Intermetallics 104 (2019) 133–142, https://doi.org/10.1016/j.intermet.2018.10.028.
[8] S. Burk, B. Gorr, H.-J. Christ, D. Schliephake, M. Heilmaier, C. Hochmuth, U. Glatzel, High-temperature oxidation behaviour of a single-phase (Mo,Ti)5Si3 (Mo–Si–Ti) alloy, Scr. Mater. 66 (2012) 223–226, https://doi.org/10.1016/j.scriptamat.2011.10.042.
[9] P. Jéhanno, M. Heilmaier, H. Saage, H. Heyse, M. Böning, H. Kestler, J. H. Schneibel, Superplasticity of a multiphase refractory Mo–Si–B alloy, Scr. Mater. 55 (2006) 525–528, https://doi.org/10.1016/j.scriptamat.2006.05.033.
[10] R. Sakidja, J.H. Perepezko, S. Kim, N. Sekido, Phase stability and structural defects in high-temperature Mo–Si–B alloys, Acta Mater. 56 (2008) 5223–5244, https://doi.org/10.1016/j.actamat.2008.07.015.
[11] M. Akinc, M.K. Meyer, M.J. Kramer, A.J. Thom, J.J. Huebsch, B. Cook, Boron-doped molybdenum silicides for structural applications, Mater. Sci. Eng. A 261 (1999) 16–23, https://doi.org/10.1016/s0921-5093(98)01045-4.
[12] M.A. Azim, B. Gorr, H.-J. Christ, O. Lenchuk, K. Albe, D. Schliephake, M. Heilmaier, Effect of Ti content and nitrogen on the high-temperature oxidation behavior of (Mo,Ti)5Si3, Intermetallics 90 (2017) 103–112, https://doi.org/10.1016/j.intermet.2017.05.023.
[13] M. Azimovna Azim, S. Burk, B. Gorr, H.-J. Christ, D. Schliephake, M. Heilmaier, R. Bornemann, P.H. Bolívar, Effect of Ti (macro-) alloying on the high-temperature oxidation behavior of ternary Mo–Si–B alloys at 820–1,300°C, Oxid. Met. 80 (2013) 231–242, https://doi.org/10.1007/s11085-013-9375-1.
[14] S. Majumdar, P.K. Singh, A.K. Pandey, G.N. Rao, Kinetics of oxide scale growth on a (Ti, Mo) 5 Si 3 based oxidation resistant Mo-Ti-Si alloy at 900–1300 ∘ C, High Temp. Mater. Process. 38 (2019) 533–540, https://doi.org/10.1515/htmp-2019-0056.
[15] S. Majumdar, B. Paul, P.K. Singh, J. Kishor, V. Kain, Effect of Si content on microstructure, mechanical and oxidation properties of hot pressed Mo-Ti-Si alloys, Intermetallics 100 (2018) 126–135, https://doi.org/10.1016/j.intermet.2018.06.013.
[16] E.F. Baroch, M. Ostermann, G. Patrick, Applications of Powder Metallurgy Molybdenum in the 1990 s vol. 5, 1991, pp. 321–331.
[17] I. Schramm Deschamps, D. dos Santos Avila, E. Vanzuita Piazera, R.C. Dudley Cruz, C. Aguilar, A.N. Klein, Design of in situ metal matrix composites produced by powder metallurgy—a critical review, Metals 12 (2022) 2073, https://doi.org/10.3390/met12122073.
[18] Y. Yang, Y.A. Chang, L. Tan, Y. Du, Experimental investigation and thermodynamic descriptions of the Mo–Si–Ti system, Mater. Sci. Eng. A 361 (2003) 281–293, https://doi.org/10.1016/S0921-5093(03)00560-4.
[19] Susanne Obert, Characterisation of the Oxidation and Creep Behaviour of Novel Mo-Si-Ti Alloys, PhD, Karlsruher, 2021.
[20] M.A. Azim, D. Schliephake, C. Hochmuth, B. Gorr, H.-J. Christ, U. Glatzel, M. Heilmaier, Creep resistance and oxidation behavior of novel Mo-Si-B-Ti alloys, JOM 67 (2015) 2621–2628, https://doi.org/10.1007/s11837-015-1560-z.
[21] M. Krüger, S. Franz, H. Saage, M. Heilmaier, J.H. Schneibel, P. Jéhanno, M. Böning, H. Kestler, Mechanically alloyed Mo–Si–B alloys with a continuous α-Mo matrix and improved mechanical properties, Intermetallics 16 (2008) 933–941, https://doi.org/10.1016/j.intermet.2008.04.015.
[22] M. Krüger, P. Jain, K.S. Kumar, M. Heilmaier, Correlation between microstructure and properties of fine grained Mo–Mo3Si–Mo5SiB2 alloys, Intermetallics 48 (2014) 10–18, https://doi.org/10.1016/j.intermet.2013.10.025.
[23] J.T. Smith, Diffusion mechanism for the nickel-activated sintering of molybdenum, J. Appl. Phys. 36 (1965) 595–598, https://doi.org/10.1063/1.1714036.
[24] K. Hwang, H. Huang, Identification of the segregation layer and its effects on the activated sintering and ductility of Ni-doped molybdenum, Acta Mater. 51 (2003) 3915–3926, https://doi.org/10.1016/S1359-6454(03)00216-7.
[25] I. Solodkyi, V. Petrusha, M.A. Grigoroscuta, J. Schmelzer, G. Hasemann, U. Betke, P. Badica, M. Krüger, Efficient sintering of mo matrix composites—a study of temperature dependences and the use of the sinter additive Ni, Metals 13 (2023) 1715, https://doi.org/10.3390/met13101715.
[26] H. Lukas, S.G. Fries, B. Sundman, Computational Thermodynamics - The Calphad Method, first ed., Cambridge University Press, New York, USA, 2007.
[27] A. Bondar, H. Lukas, A. Czerny, V. Romaka, Mo-Si-Ti ternary phase diagram evaluation, MSI Eureka 97 (2023), https://doi.org/10.7121/msi-eureka-10.18571.2.8, 10.18571.2.8.
[28] A. Watson (Ed.), Refractory metal systems: Molybdenum – Titanium – Zirconium, Springer Materials, Stuttgart, Germany, 2010.
[29] G. Winkens, A. Kauffmann, J. Herrmann, A.K. Czerny, S. Obert, S. Seils, T. Boll, C. Baruffi, Y. Rao, W.A. Curtin, R. Schwaiger, M. Heilmaier, The influence of lattice misfit on screw and edge dislocation-controlled solid solution strengthening in Mo-Ti alloys, Commun. Mater. 4 (2023) 26, https://doi.org/10.1038/s43246-023-00353-8.
[30] S. Obert, A. Kauffmann, M. Heilmaier, Characterisation of the oxidation and creep behaviour of novel Mo-Si-Ti alloys, Acta Mater. 184 (2020) 132–142, https://doi.org/10.1016/j.actamat.2019.11.045.
[31] D. Sturm, M. Heilmaier, J.H. Schneibel, P. Jéhanno, B. Skrotzki, H. Saage, The influence of silicon on the strength and fracture toughness of molybdenum, Mater. Sci. Eng. A 463 (2007) 107–114, https://doi.org/10.1016/j.msea.2006.07.153.
[32] I. Rosales, J. Schneibel, Stoichiometry and mechanical properties of Mo3Si, Intermetallics 8 (2000) 885–889, https://doi.org/10.1016/S0966-9795(00)00058-3.
[33] P.R. Bergethon, E.R. Simons, Flow in a Chemical Potential Field: Diffusion, in: P. R. Bergethon, E.R. Simons (Eds.), Biophysical Chemistry, Springer, New York, New York, NY, 1990, pp. 225–234.
[34] I. Solodkyi, V. Mosiichuk, O. Kucher, M. Krüger, Synthesis and spark plasma sintering of Ti5Si3-Mo powders with core-shell structure, Vacuum 232 (2025) 113843, https://doi.org/10.1016/j.vacuum.2024.113843.
[35] M. Tokita, Progress of spark plasma sintering (sps) method, systems, ceramics applications and industrialization, Ceramics 4 (2021) 160–198, https://doi.org/10.3390/ceramics4020014.

[36] M. Teslia, S. Teslia, I. Solodkyi, Synthesis of Mo–Ti–Ta–Cr alloy powders by calciothermic reduction, JMMP 10 (2026) 251, https://doi.org/10.3390/jmmp10070251.
[37] J. Schneibel, C. Rawn, Thermal expansion anisotropy of ternary titanium silicides based on Ti5Si3, Acta Mater. 52 (2004) 3843–3848, https://doi.org/10.1016/j.actamat.2004.04.033.
[38] M. Zhao, S. Nakayama, T. Hatakeyama, J. Nakamura, K. Yoshimi, Microstructure, high-temperature deformability and oxidation resistance of a Ti5Si3-containing multiphase MoSiBTiC alloy, Intermetallics 90 (2017) 169–179, https://doi.org/10.1016/j.intermet.2017.07.018.
[39] D. Schliephake, S.R. Ramdoss, R.J. Vikram, G. Falcão, F. Galgon, H. Thota, F. Hinrichs, C. Zenk, A. Kauffmann, Y. Eggeler, S. Suwas, R. Schwaiger, M. Heilmaier, Microstructure and mechanical properties of a laser-based directed energy deposited Mo-Si-Ti alloy, J. Mater. Sci. 60 (2025) 18246–18260, https://doi.org/10.1007/s10853-025-11158-0.
[40] P. Jéhanno, M. Böning, H. Kestler, M. Heilmaier, H. Saage, M. Krüger, Molybdenum alloys for high temperature applications in air, Powder Metall. 51 (2008) 99–102, https://doi.org/10.1179/174329008X313379.
[41] A.P. Alur, N. Chollacoop, K.S. Kumar, High-temperature compression behavior of Mo–Si–B alloys, Acta Mater. 52 (2004) 5571–5587, https://doi.org/10.1016/j.actamat.2004.08.035.